

DRAFT VERSION DECEMBER 7, 2023

Typeset using L^AT_EX preprint style in AASTeX631

X-ray Observations of the Enigmatic Wolf-Rayet System θ Mus: Two's Company But Three's a Crowd

STEPHEN L. SKINNER,¹ SVETOZAR A. ZHEKOV,² MANUEL GÜDEL,³ AND WERNER SCHMUTZ⁴

¹*Center for Astrophysics and Space Astronomy (CASA), University of Colorado, Boulder, CO, USA 80309-0389*

²*Inst. of Astronomy and National Astronomy Observatory, Bulgarian Academy of Sciences, 72 Tsarigradsko Chaussee Blvd., Sofia, 1784, Bulgaria*

³*Dept. of Astrophysics, Univ. of Vienna, Türkenschanzstr. 17, A-1180 Vienna, Austria*

⁴*Physikalisch-Meteorologisches Observatorium Davos and World Radiation Center (PMOD/WRC), Dorfstrasse 33, CH-7260 Davos Dorf, Switzerland*

(Accepted 4 December 2023)

Submitted to ApJ

ABSTRACT

θ Mus is a remarkable spectroscopic binary (SB) consisting of a carbon-type Wolf-Rayet star and OV companion (WC6+O6-7V) in a ≈ 19 -day orbit. In addition an O-supergiant is visually detected at a small offset of 46 mas and if gravitationally bound to the SB system would have an orbital period of many decades. θ Mus is X-ray bright and a nonthermal radio source as commonly observed in massive colliding wind (CW) binaries. We present new *Chandra* X-ray observations of θ Mus which complement previous *XMM-Newton* observations. The X-ray emission consists of a cool nearly steady weakly-absorbed plasma component with broad redshifted emission lines located in an extended region far from the SB system. Hotter plasma is also present traced by Fe XXV emission. The observed flux in the ≈ 2 -5 keV range dropped significantly on a timescale of ≤ 5 years. The flux decrease can be attributed to an increase in absorption toward the hotter plasma which is likely located in the confined wind interaction region of the short-period SB system. The X-ray emission of θ Mus is remarkably similar to the WC+O binary γ^2 Vel including carbon recombination spectral lines but both systems show unusual line centroid properties that challenge CW models.

Corresponding author: Stephen L. Skinner
stephen.skinner@colorado.edu

1. INTRODUCTION

Wolf-Rayet (WR) stars are evolved massive stars that may end their lives as supernovae, in some cases accompanied by γ -ray bursts (Woosley & Bloom 2006). They are losing mass at high rates and their powerful winds replenish the interstellar medium with metal-rich material that will be recycled into new generations of stars. With typical terminal wind speeds $V_\infty \approx 1000 - 2500 \text{ km s}^{-1}$, the supersonic winds of WR stars and interacting winds in massive WR+OB binaries offer excellent opportunities for observational tests of wind shock models.

The present work focuses on X-ray properties of the multiple system θ Mus (= HD 113904 = WR 48). It is a spectroscopic binary (SB) consisting of a carbon-type WR star with an O-star companion (WC6+O6-7V) in a 19-day orbit. In addition an O9.5I star is visually detected at an offset of 46 ± 9 mas (Hartkopf et al. 1999). *Chandra* has an angular resolution of about one arcsecond which is not sufficient to spatially resolve the two components of the θ Mus SB system or disentangle emission of the SB system from that of the O supergiant. X-rays in such multiple systems can arise in the shocked winds of either star or in colliding wind (CW) shocks formed between the stars. Thus, the observed X-ray spectrum may consist of multiple superimposed components. Distinguishing between them relies on diagnostics such as plasma temperature distribution and emission line properties (e.g. line widths, centroid shifts). Reliable measurements of line properties require high spectral resolution grating observations.

X-rays can be produced in the winds of the individual stars in massive binaries as a result of radiative shocks associated with line-driven instabilities (Lucy & White 1980; Owocki et al. 1988; Feldmeier et al. 1997). Radiative shocks are predicted to generate cool X-ray plasma ($kT \lesssim 1 \text{ keV}$) as has been observed in objects like the O4I star ζ Puppis (Cassinelli et al. 2001; Kahn et al. 2001). But single nitrogen-type WN stars without known companions reveal hotter plasma ($kT \gtrsim 2 \text{ keV}$) that is not predicted for radiative wind shocks (Skinner et al. 2010; 2012) as do rare oxygen-type WO stars (Sokal et al. 2010; Skinner et al. 2019). But it is remarkable that putatively single carbon-type WC stars with tremendous bolometric luminosities and powerful winds have so far eluded X-ray detection in sensitive pointed observations (Oskinova et al. 2003; Skinner et al. 2006).

Hot X-ray plasma can arise in CW shocks in WR+OB systems (Cherapashchuk 1976; Prilutskii & Usov 1976; Luo et al. 1990; Usov 1992; Stevens, Blondin, & Pollock 1992). The predicted maximum temperature for an adiabatic CW shock is $kT_{cw} \approx 1.96\mu[V_\perp/1000 \text{ km s}^{-1}]^2 \text{ keV}$ where μ is the mean particle weight in the wind and V_\perp is the wind velocity component perpendicular to the shock front (Luo et al. 1990). For terminal wind speeds $V_\infty \approx 1000 - 2500 \text{ km s}^{-1}$ typical of WR and O stars maximum shock temperatures on the line-of-centers $kT_{cw} \gtrsim 2 \text{ keV}$ are expected. Such hotter plasma has now been detected in several WR binaries. These include well-studied systems like the 78-day binary γ^2 Vel whose whose WC8+O7.5 type is similar to θ Mus (Willis, Schild, & Stevens 1995; Skinner et al. 2001; Schild et al. 2004).

We present here new *Chandra* X-ray observations of the multi-component WR system θ Mus when the O6-7V star was passing in front of the WR star ($\phi \approx 0.6$). In addition we summarize archived *XMM-Newton* data obtained in 2004 at nearly the same phase as *Chandra* and in 2009 ($\phi \approx 0.95$) with the WR star passing in front. The primary objective was to confirm and extend previous reports of redshifted emission lines and attempt to reconcile the observed X-ray emission with the CW shock interpretation.

2. THE TARGET: θ MUS

θ Mus (= HD 113904) is listed as WR 48 in the catalog of van der Hucht (2001) with a visual extinction $A_v = 0.93$ mag. This equates to $A_V = 0.84$ mag using $A_V = 0.9A_v$. Its *Gaia* DR3 parallax distance is 2.168 kpc. The SB system was classified as WC6+O6-7V by Hill et al. (2002).

To determine orbital phases of the X-ray observations we use the orbital solution for the SB system of Hill et al. (2002) who adopted a period $P_{orb} = 19.1375 \pm 0.0025$ d based on the work of Schnurr (1999). But the determination of the SB orbital parameters is hampered by the nearby bright supergiant. No atmospheric eclipse that could be used to constrain the orbital ephemeris has so far been detected in the SB system (Lenoir-Craig et al. 2021). Lenoir-Craig et al. also note an unexplained phase difference for time of minimum brightness between their results and those of Marchenko et al. (1998). Attempts to quantify the SB orbit based on linear polarization observations have yielded negative results (St.-Louis et al. 1987). Moffat & Seggewiss (1977) determined $P_{orb} = 18.341 \pm 0.008$ d, but aliasing also allows values of 18.596 d, 18.858 d, or 19.128 d (Lenoir-Craig et al. 2021). Using *Hipparcos* photometry Marchenko et al. (1998) obtained $P_{orb} = 18.05 \pm 0.32$ d. Considering the above mixed results, the X-ray orbital phases computed using $P_{orb} = 19.1375$ d (Tables 1,2) should be treated with caution.

If the OI star is gravitationally bound to the SB system at the *Gaia* DR3 parallax distance of 2.17 kpc then a long-period orbit is predicted. The 46 mas offset corresponds to a *projected* separation $D_{proj} \approx 100$ AU. To estimate the orbital period we assume a WR mass $M_{WC6} = 12 M_{\odot}$ (Hill et al. 2002) and O-star masses (Weidner & Vink 2010) $M_{O7V} = 30 M_{\odot}$ and $M_{O9.5I} = 35 M_{\odot}$. To simplify the three-body orbit to a tractable two-body orbit we combine the SB system into a single object of mass $\approx 42 M_{\odot}$. This combined mass is similar to the OI star mass and the center-of-mass thus lies approximately halfway between the SB system and the OI star. If the orbit of the OI+SB system is near-circular their physical (deprojected) separation D is twice the orbit semi-major axis a . Since $D \geq D_{proj}$ we obtain $a \geq 50$ AU and by Kepler's 3rd law $P_{orb,OI} \geq 40$ years. This is a lower limit and the actual period, which depends on the (unknown) *deprojected* separation D , could be much longer than 40 years. Previous nonthermal radio studies have argued that the OI star is in such a bound orbit (Dougherty & Williams 2000).

3. PREVIOUS *XMM-NEWTON* OBSERVATIONS

An X-ray observation of θ Mus with *XMM-Newton* was obtained in 2004 (ObsId 0090030201) when the OI star was nearly in front of the WR star and analyzed by Sugawara et al. (2008). A second *XMM-Newton* observation in 2009 (ObsId 0605670201) at nearly opposite phase is archived and discussed below. Somewhat surprisingly, bright low-temperature emission lines such as O VIII (maximum line power at $T_{max} \approx 3$ MK) in the *XMM-Newton* grating spectrum were found to be redshifted by ≈ 650 km s $^{-1}$ when the O6-7V star was passing in front. If the X-ray emission originates in a CW shock in the SB system and the WR wind momentum dominates the O6-7V wind (as is usually the case) then blueshifted lines would be expected when the O6-7V star is passing in front of the WR star. In that viewing geometry the CW shock cone wraps around the O6-7V star with a blueshifted flow velocity component toward the observer. The magnitude of the blueshift depends on the shock cone opening angle with wider angles giving smaller blueshifts. To explain the puzzling redshifted lines, Sugawara et al. (2008) proposed that they originate in a CW shock between the SB

Table 1. θ Mus X-ray Properties (Chandra ACIS-S/HETG 0-order)

ObsId	Start Date/Time	Livetime	Phase ^a	Counts	Count rate	E ₅₀	H.R.	P _{var}
	TT	(ks)		(cts)	(cts ks ⁻¹)	(keV)		
23378	2020 Nov 24 10:39	14.757	0.60-0.61	189	12.56±2.98	2.60	0.67	0.06
24869	2020 Nov 24 23:16	14.755	0.63-0.64	211	13.91±3.11	2.83	0.79	0.12
24497	2022 Jun 1 19:25	29.574	0.57-0.59	259	8.63±2.99	2.79	0.71	0.09
24498	2022 Jun 3 06:03	30.393	0.64-0.66	408	13.17±2.48	2.64	0.74	0.06
24496	2022 Jun 22 13:14	29.575	0.65-0.67	345	11.60±3.71	2.63	0.74	0.05
mean	11.97±1.83	2.70	0.73	...

NOTE— The livetime is the on-source time and excludes dead-time when the detector is not collecting data. X-ray properties are based on source events in the 0.2 - 8 keV range. The mean count rates and standard deviations were obtained by fitting the X-ray light curve binned at 1200 s intervals. E₅₀ is the median photon energy. Hardness ratio H.R. = counts(2-8 keV)/counts(0.2-8 keV). P_{var} is the probability that the source is variable based on event arrival times as determined by the CIAO tool *glvary*. The X-ray centroid position obtained by averaging all observations is (J2000) R.A. = 13h 08m 07.140s Decl. = -65° 18' 21.70". The *Hubble Space Telescope (HST)* Guide Star Catalog (GSC v2.3.2) position of θ Mus is R.A. = 13h 08m 07.155s Decl. = -65° 18' 21.50". The 2MASS position is R.A. = 13h 08m 07.153s Decl. = -65° 18' 21.517".

^aThe start-stop phases are referenced to phase $\phi = 0$ (WR star in front) at $T_o = \text{HJD } 2451377.51 \pm 0.45$ d and assume an orbital period $P_{orb} = 19.1375 \pm 0.0025$ d (Hill et al. 2002).

system and the OI star. In that picture the OI star would be in a bound orbit with the SB system and behind it (Fig. 4 of Sugawara et al. 2008).

4. X-RAY OBSERVATIONS

4.1. *Chandra*

The total *Chandra* observing time (≈ 120 ks) was split into five segments (Table 1) to accommodate *Chandra*'s operational constraints. The data were obtained using the High Energy Transmission Grating (HETG)/Advanced CCD Imaging Spectrometer (ACIS-S) combination. The HETG provides grating data from the Medium Energy Grating (MEG) and High Energy Grating (HEG). ACIS-S also gives undispersed HETG 0-order data (hereafter referred to as ACIS-S 0-order or simply ACIS-S) at lower energy resolution than HETG. Detailed information on *Chandra*'s instrumentation is in the Proposer's Observatory Guide (POG)¹.

The pipeline-processed data files provided by the *Chandra* X-ray Center were analyzed using science threads in *Chandra* Interactive Analysis Software (CIAO version 4.14) and recent calibration data (CALDB version 4.9.8). ACIS-S 0-order source events were extracted from a circular region of radius 2.''0 centered on the X-ray peak for each observation. Background is negligible. Energy-filtered 0-order source events were used to determine count rates, median event energies, and hardness ratios (H.R.). The probability of source variability was determined using the CIAO tool *glvary*. CIAO *specextract* was used to extract ACIS-S 0-order spectra for each observation along with observation-specific response matrix files (RMFs) and auxiliary response files (ARFs). Spectral fitting was undertaken with CIAO *Sherpa* and HEASOFT XSPEC version 12.8.2². The ACIS-S 0-order spectra for

¹ <https://cxc.harvard.edu/proposer/POG/>

² <http://heasarc.gsfc.nasa.gov/xanadu/xspec>

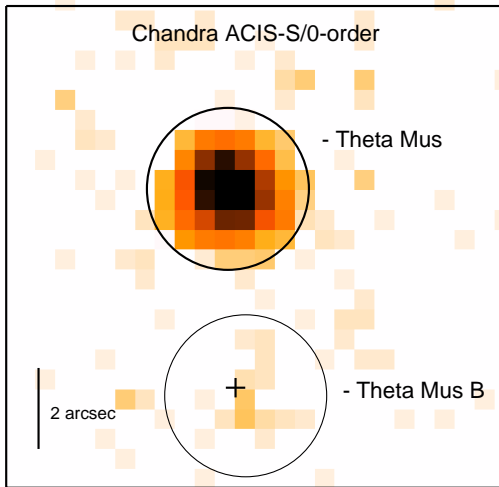


Figure 1. *Chandra* image from summed June 2022 observations (0.2-8 keV; $0''.49$ pixels; 89.54 ks livetime). Circles ($2''$ radii) are centered on X-ray centroids. Cross (+) marks the optical position of θ Mus B which is likely the faint X-ray source (16 cts). N up, E left.

the five observations were fitted simultaneously in XSPEC, the recommended procedure for analyzing *Chandra* data acquired at different epochs. The five spectra were combined into a single spectrum for display purposes. To facilitate comparison with the results of Sugawara et al. (2008) we have modeled X-ray absorption using the XSPEC *wabs* model. Fits were compared with the more recent *tbabs* absorption model and only minor differences were found.

We analyzed 1st order MEG1 and HEG1 grating spectra (+1 and -1 orders combined). The MEG1 spectra for each observation were combined into a summed MEG1 spectrum using CIAO *combine_grating_spectra*, and similarly for HEG1. Grating RMF and ARF files were generated using CIAO *mktgresp*. Emission lines were fitted with Gaussian profiles to determine line properties. Since the grating spectra of the individual observations do not contain enough line counts to reliably measure line properties the summed grating spectra were used for line fitting.

4.2. XMM-Newton

For comparison with *Chandra* we have retrieved the *XMM-Newton* archive data for the two θ Mus observations, ObsIds 0090030201 (119.6 ks, 20 July 2004) and 0605670201 (54.3 ks, 19 July 2009). The data were reprocessed using the *XMM-Newton* Science Analysis Software (SAS vers. 18) modules *epchain* and *emchain*, applying recent calibration data. Undispersed source spectra were extracted using SAS *xmmselect* for the pn, MOS1, and MOS2 detectors comprising the European Photon Imaging Camera (EPIC). Background spectra were extracted in adjacent source free regions. Observation-specific RMF and ARF files were created for each EPIC spectrum using SAS modules *rmfgen* and *arfgen*. Spectra were fitted using XSPEC as for the *Chandra* data.

5. RESULTS

5.1. Chandra

θ Mus was clearly detected in all five *Chandra* observations (Table 1). Figure 1 shows the ACIS-S 0-order image obtained by combining events from the June 2022 observations. A faint X-ray source lies $5''.2$ south of θ Mus whose X-ray centroid is offset $0''.35$ from the O9III star θ Mus B. This offset

is well within the 1σ *Chandra* ACIS-S absolute astrometric accuracy of $0''.79$ (68% confidence circle radius³). so the faint source is most likely θ Mus B. Its count rate is more than 60 times lower than θ Mus. The $r = 2''$ extraction region used for θ Mus ACIS-S analysis excludes the faint emission from θ Mus B which is not of primary interest in this study. The X-ray centroid is in excellent agreement with optical and near-IR positions of θ Mus. The X-ray properties in Table 1 are similar for each observation. The individual observations show no significant X-ray variability but the count rate in ObsId 24497 is 1.8σ lower than the mean for all five observations. If real, this decrease would indicate variability on a short timescale of ≤ 2 days.

Undispersed ACIS-S Spectra. The summed ACIS-S spectrum is shown in Figure 2-top. As noted, the individual spectra were fitted simultaneously in XSPEC. We compared fits using two-temperature optically thin plasma models (2T *vaptec*) and 2T plane-parallel shock models (2T *vpshock*) which are typically used for modeling WR star X-ray spectra. The *vaptec* model assumes collisional ionization equilibrium (CIE) whereas the *vpshock* model accounts for possible non-equilibrium ionization (NEI) conditions that may occur in the plasma of rapidly-heated shocks (e.g. Zhekov 2007).

To make comparisons with the analysis of *XMM-Newton* spectra by Sugawara et al. (2008) we referenced the abundances in spectral fits (Table 2) to the solar values of Anders & Grevesse (1989). But evolved WC stars have nonsolar abundances that are depleted in hydrogen and nitrogen with enhanced carbon. We have thus compared solar abundance spectral fits with fits using generic WC star abundances (van der Hucht, Cassinelli, & Williams 1986). The fit quality as judged by χ^2 is poor using the generic WC abundances but improves by allowing the C abundance to increase above the generic reference value, as was also true for fits referenced to solar abundances.

The 2T *vpshock* model provides slightly better fits of the ACIS-S spectra than 2T *vaptec* as gauged by the χ^2 fit statistic. Thus we do not include the ACIS-S 2T *vaptec* fit in Table 2 but it is included for the higher signal-to-noise ratio 2009 *XMM-Newton* EPIC data (discussed below). Even so, both models converge to similar values for physical quantities such as plasma temperature. The ACIS-S spectra do not tightly constrain the absorption column density so it was held fixed in ACIS-S fits at $N_{\text{H}} = 1.6 \times 10^{21} \text{ cm}^{-2}$, consistent with that expected for $A_{\text{V}} = 0.84$ and a standard conversion $N_{\text{H}} (\text{cm}^{-2}) = 1.9 \pm 0.3 \times 10^{21} \cdot A_{\text{V}}$ (Gorenstein 1975; Vuong et al. 2003). It is also nearly identical to that obtained from 2T *vpshock* fits of *XMM-Newton* EPIC spectra (Table 2).

The various ACIS-S spectral fits show very little sensitivity to abundance deviations from solar, which is not surprising given the moderate spectral resolution of ACIS-S and the modest number of spectral counts. However all fits converged to a subsolar Fe abundance, as was also found in our analysis of *XMM-Newton* spectra below and by Sugawara et al. (2008). The carbon and oxygen lines present in *XMM-Newton* spectra at energies below 0.7 keV lie below the energy range where ACIS-S is sensitive. Thus *Chandra* does not provide any constraints on the C abundance although *XMM-Newton* spectra do (Sec. 5.2).

HETG Spectra. The *Chandra* MEG1 spectrum of θ Mus is shown in Figure 3-top. Several emission lines and line blends are present (Table 3) spanning a temperature range of $T_{\text{max}} \approx 6$ MK (Ne X) to $T_{\text{max}} \approx 16$ MK (S XV). The HEG1 spectrum is similar to MEG1 but only the Mg XII, Si XIII, and S XV lines in HEG1 have sufficient counts to permit line measurements. Even so, they provide a

³ <https://cxc.harvard.edu/cal/ASPECT/celmon/>

good cross-check with MEG1 since HEG1 spectral resolution ($\Delta\lambda = 0.012 \text{ \AA}$) is superior to MEG1 ($\Delta\lambda = 0.023 \text{ \AA}$).

All of the HETG lines are redshifted with exception of S XV (Table 3). The Ne X line (12 net MEG1 counts) has a redshift of +841 (−396,+593) km s^{-1} and width FWHM $\approx 0.04 \text{ \AA}$ ($\approx 990 \text{ km s}^{-1}$). This width is nearly twice the MEG1 resolving power. Line broadening is also present in the *XMM-Newton* grating spectra (Sugawara et al. 2008).

Table 3 shows what appears to be a trend toward smaller redshifts in hotter lines. The individual components of the doublet lines (Ne X, Mg XII, Si XIV) are not resolved by MEG1 and their redshifts may be slightly overestimated due to flux contributions from the weaker longer wavelength component. These doublets appear somewhat broadened in the MEG1 spectrum. The faint Si XIV line (2.006 keV) is too noisy to permit a reliable centroid measurement. The S XV line (12 net MEG1 counts) is uncontaminated by other lines and quite sharp. Its measured centroid is $\lambda_{obs} = 5.039 (-0.007, +0.006; 1\sigma) \text{ \AA}$ or $v = 0 (-417, +357) \text{ km s}^{-1}$. The uncertainty is within the limits of MEG1 absolute wavelength calibration accuracy of $\pm 0.011 \text{ \AA}$. Thus, we measure no significant centroid shift in this hotter S XV line.

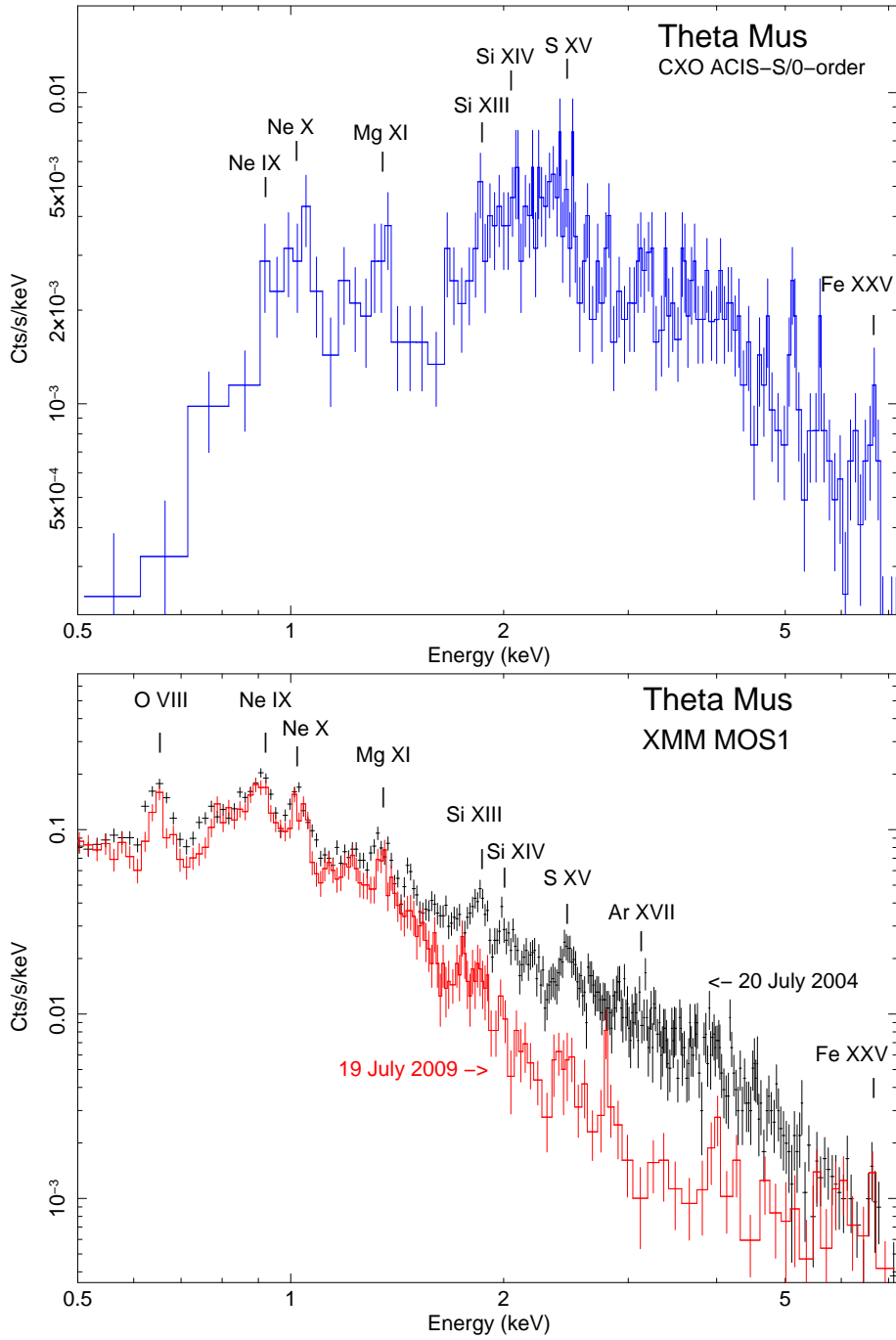


Figure 2. Background-subtracted X-ray spectra of θ Mus (log-log scale). *Top:* Summed *Chandra* ACIS-S 0-order (1430 cts; minimum 3 cts/bin). The feature at 5.1 keV is unidentified. *Bottom:* XMM-Newton MOS1 (minimum 10 cts/bin) for ObsIds 0090030201 (black; 18903 cts) and 0605670201 (red; 6458 cts).

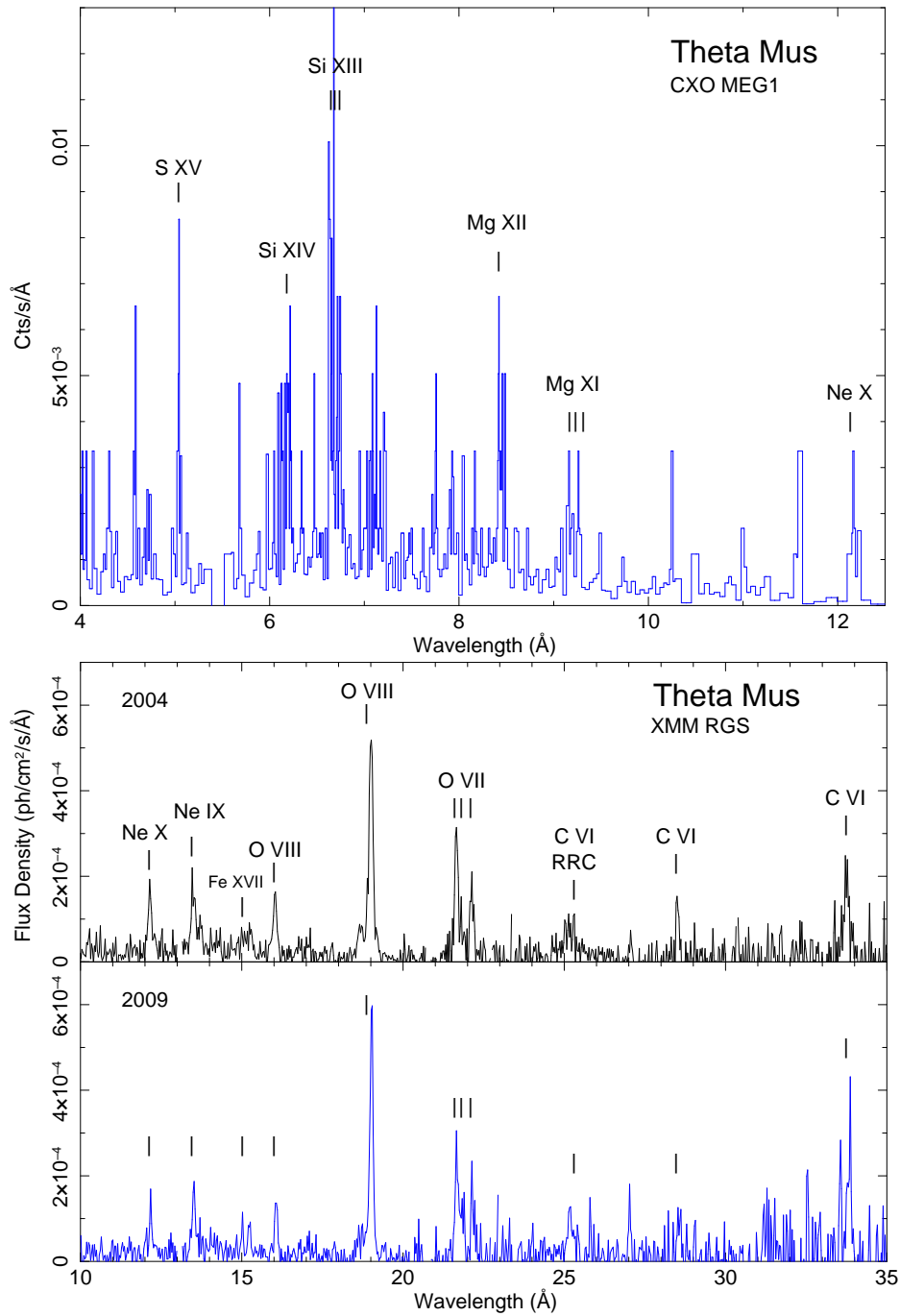


Figure 3. θ Mus 1st order grating spectra. ATOMDB line lab wavelengths are marked. *Top:* Summed *Chandra* MEG1 (1188 cts; lightly rebinned). Error bars omitted for clarity. *Bottom:* *XMM-Newton* RGS1+RGS2 (bin width of 0.03 Å) for ObsIds 0090030201 (black) and 0605670201 (blue).

Table 2. Spectral Fits of θ Mus

Parameter	Chandra	XMM-Newton	XMM-Newton	XMM-Newton
Instrument	ACIS-S/0-order	EPIC (pn+MOS)	EPIC (pn+MOS)	EPIC (pn+MOS)
ObsId	all	0090030201	0090030201	0605670201
Year	2020, 2022	2004	2004	2009
Phase (ϕ)	0.58 - 0.66	0.60 - 0.67	0.60 - 0.67	0.95 - 0.98
Model ^a	2T <i>vpshock</i>	2T <i>vpshock</i>	2T <i>vapec</i>	2T <i>vpshock</i>
Abundances	varied ^b	varied ^c	varied ^d	varied ^e
N _{H,1} (10 ²² cm ⁻²)	(0.16)	0.16 [0.15 - 0.18]	0.13 [0.12 - 0.14]	(0.16)
N _{H,2} (10 ²² cm ⁻²)	17.1 [15.2 - 19.7]
kT ₁ (keV)	(0.40)	0.51 [0.50 - 0.53]	0.37 [0.36 - 0.38]	0.79 [0.77 - 0.81]
kT ₂ (keV)	4.67 [4.26 - 5.23]	4.34 [4.27 - 4.48]	4.04 [3.94 - 4.14]	(4.3)
E _{edge} (keV)	... ^f	0.55 [0.54 - 0.56]	0.56 [0.55 - 0.57]	0.54 [0.54 - 0.55]
kT _{edge} (eV)	... ^f	4.0 [0.5 - 6.7]	3.5 [1.8 - 5.5]	(4.0)
redshift ^f	(0)	(2.17e-3)	(2.17e-3)	(2.17e-3)
norm ₁ /norm ₂	0.55	1.05	1.57	1.86
$\tau_{u,1}$ (s cm ⁻³)	2.32e+10	3.89e+11	...	4.63e+11
$\tau_{u,2}$ (s cm ⁻³)	4.67e+13	15.5e+11 ^g
χ^2/dof (χ^2_{red})	314.8/255 (1.23)	2519.7/2281 (1.10)	2668.9/2285 (1.17)	1241.2/1149 (1.08)
F _{X,abs} ^h	12.5 [10.6 - 14.0] ⁱ	16.06 [15.90 - 16.10]	16.01 [15.90 - 16.06]	10.1 [10.0 - 10.2]
F _{X,2,abs} ^h	6.10	8.87	8.75	1.06
log L _X (ergs s ⁻¹)	33.31	33.36	33.23	33.31

NOTE— Based on XSPEC simultaneous fits of binned background-subtracted spectra. The tabulated parameters are absorption column density (N_H), plasma temperature in energy units (kT), ratio of cool/hot plasma normalizations (norm₁/norm₂), emission-recombination edge threshold energy (E_{edge}) and temperature in energy units (kT_{edge}), upper limit on ionization timescale (τ_u), total absorbed X-ray flux (F_{X,abs}), hot component absorbed X-ray flux (F_{X,2,abs}), and unabsorbed X-ray luminosity L_X at d = 2.168 kpc. X-ray fluxes and L_X are evaluated in the 0.2-8 keV range. Square brackets enclose 1 σ confidence intervals. Values in parentheses were held fixed during fitting. Abundances are fixed at the solar values of Anders & Grevesse (1989) except as noted below.

^a 2T *vpshock* model for *Chandra* ACIS-S and *XMM-Newton* EPIC 2004 fits use one absorption component and are of form $wabs_1 \cdot (redge + vpshock_1 + vpshock_2)$ where $wabs_1 \equiv N_{H,1}$. The EPIC 2009 fit includes a second absorption component $wabs_2 \equiv N_{H,2}$ that is varied independently and is of form $wabs_1 \cdot (redge + vpshock_1) + wabs_2 \cdot vpshock_2$. 2T *vapec* model is of form $wabs_1 \cdot (redge + vapec_1 + vapec_2)$.

^b Varied abundances and best-fit values are Fe = 0.27 [0.13 - 0.41] \times solar.

^c Varied abundances and best-fit values are C = 4.34 [3.27 - 5.71], O = 0.42 [0.40 - 0.48], Ne = 0.74 [0.73 - 0.84], Mg = 0.37 [0.36 - 0.43], Si = 1.14 [1.09 - 1.24], S = 2.18 [2.03 - 2.32] Fe = 0.11 [0.10 - 0.14] \times solar.

^d Varied abundances and best-fit values are C = (4.34) fixed, O = 0.63 [0.60 - 0.68], Ne = 0.99 [0.93 - 1.07], Mg = 0.46 [0.40 - 0.52], Si = 2.54 [2.38 - 2.70], S = 3.30 [3.01 - 3.60] Fe = 0.10 [0.09 - 0.11] \times solar.

^e Varied abundances and best-fit values are C = 7.99 [7.58 - 9.33], O = 0.60 [0.54 - 0.67], Ne = 0.50 [0.46 - 0.55], Mg = 0.39 [0.35 - 0.44], Fe = 0.12 [0.11 - 0.14] \times solar.

^f ACIS-S fits are not sensitive to *redshift* or *redge*. For EPIC fits redshift was held fixed at [2.17e-3] = 650 km s⁻¹ (Sugawara et al. 2008).

^g Fit did not converge to a stable value.

^h Flux (0.2-8 keV) is in units of 10⁻¹³ ergs cm⁻² s⁻¹.

ⁱ *Chandra* ACIS-S 0-order has low effective area below \approx 1 keV compared to *XMM-Newton* EPIC (Sec. 5.2).

Table 3. θ Mus Spectral Lines

Ion	E_{lab} (keV)	λ_{lab} (Å)	λ_{obs} (Å)	$\Delta\lambda$ (Å [km s ⁻¹])	log T_{max} (K)	Net Line Flux (10 ⁻⁶ ph cm ⁻² s ⁻¹)
XMM-Newton (RGS)						
O VIIr	0.574	21.602	21.663 (2004)	+0.061 [+847]	6.3	3.73
O VIIr	0.574	21.602	21.679 (2009)	+0.068 [+944]	6.3	3.52
O VIII	0.654	18.967/18.973 ^a	19.010 (2004)	+0.043 [+680]	6.5	7.61
O VIII	0.654	18.967/18.973 ^a	19.025 (2009)	+0.058 [+917]	6.5	6.90
Chandra (HETG1)						
Ne X	1.022	12.132/12.137 ^a	12.166 (MEG)	+0.034 [+841]	6.8	9.95
Mg XII	1.473	8.419/8.425 ^a	8.437 (HEG)	+0.018 [+641]	7.0	1.87
Si XIIIr	1.865	6.648	6.655 (MEG)	+0.007 [+316]	7.0	2.09
Si XIIIf	1.840	6.740	6.746 (MEG)	+0.006 [+267]	7.0	1.51
S XV	2.460	5.039	5.039 (MEG,HEG)	0 [0]	7.2	3.70

Notes: Laboratory wavelengths (λ_{lab}) and maximum line power temperatures (T_{max}) are from the ATOMDB database (www.atomdb.org). Line measurements are based on the summed MEG1 spectra from all five observations except for Si XIIIr (resonance) and Si XIIIf (forbidden) lines which were only measurable in ObsIds 24497 and 24498. Net photon (ph) line fluxes are continuum-subtracted. Typical flux uncertainties are 20%.

^aBlended doublet.

5.2. XMM-Newton

We compare here the *XMM-Newton* spectra with *Chandra*. The comparison is useful because *XMM-Newton* provides better low-energy sensitivity and spectra were obtained at nearly the same phase as *Chandra* and at opposite phase where *Chandra* data are lacking.

Undispersed EPIC Spectra. Figure 2-bottom shows EPIC MOS1 spectra for both *XMM-Newton* observations. These spectra give reliable broad-band fluxes and estimates of basic spectral parameters (N_{H} , kT). Table 2 compares fits of the EPIC and *Chandra* ACIS-S 0-order spectra. The 2T *vpshock* fits of the ACIS-S and 2004 EPIC spectrum obtained at about the same phase give similar results but the ACIS-S fits place less emission measure in the cooler plasma component. This is largely due to the lower ACIS-S sensitivity at energies below 1 keV. This difference is apparent in Figure 2 which reveals significant emission below ≈ 1 keV in the MOS spectra such as the O VIII line which is not detected by *Chandra*. Thus, ACIS-S fits yield a lower measured flux than EPIC at $\phi \approx 0.65$ (Table 2). EPIC spectral fits are slightly improved in the range 0.49 - 0.55 keV near the C VI radiative recombination continuum (RRC) feature by including a recombination edge (*redge*) component as did Sugawara et al. (2008). The RRC feature is faint in the EPIC spectra but clearly visible in RGS. The *redge* component does not affect ACIS-S fits since ACIS-S detects very little flux near 0.5 keV.

Table 2 includes a fit of the 2004 EPIC spectra using a 2T *vapec* optically thin plasma model for comparison with 2T *vpshock*. The two models give similar results but 2T *vpshock* yields a slightly higher absorption N_{H} and thus a higher L_x . Also the 2T *vpshock* model converges to a more stable value of the C abundance which is above solar and consistent with that obtained from 2T *vpshock* fits by Sugawara et al. (2008).

The 2009 *XMM-Newton* observation at phase $\phi = 0.95 - 0.98$ provides crucial variability information. At lower energies the 2009 EPIC spectrum is quite similar to the 2004 EPIC spectrum but a modest flux change of $\leq 20\%$ below 1.5 keV is not ruled out. More obvious is the decrease in emergent flux at higher energies $E \approx 2 - 5$ keV in the 2009 EPIC spectrum, but little if any change at the Fe XXV energy (6.67 keV). Fits of the 2009 EPIC spectra give an absorbed broad-band flux $F_{x,abs}(0.2-8 \text{ keV}) = 9.85 [9.41 - 10.1] \times 10^{-13} \text{ ergs cm}^{-2} \text{ s}^{-1}$. This is only 61% of the 2004 value. The hard-band (2-8 keV) flux dropped by more than a factor of 3 compared to the 2004 observation and accounts for most of the change. The emission measure and observed flux in the 2009 observation are dominated by the cooler plasma component. Even so, hot plasma traced by Fe XXV ($T_{max} \approx 63 \text{ MK}$) is also present but the 2009 EPIC spectra do not tightly constrain the hot-component temperature.

The decrease in hard-band flux could be due to a change in the intrinsic X-ray spectrum or an increase in the absorption of the hotter plasma component. Although some intrinsic spectral change is not excluded an increase in absorption due to a change in viewing geometry over orbital phase is more easily reconciled with the CW picture. In that interpretation higher absorption is expected when the WR star passes in front ($\phi \approx 0$) and the line-of-sight toward the hottest CW shock plasma near the line-of-centers passes through the dense metal-enriched WR wind. Lower absorption is anticipated when the OV star passes in front ($\phi \approx 0.5$) and the hotter CW shock plasma is viewed through a low-density cavity formed by the OV star wind.

To test this hypothesis a separate absorption component ($N_{\text{H},2}$) was applied to the hotter plasma component in the 2T *vpshock* model of the 2009 EPIC spectra. This model provides a good fit (Table 2) and requires high but loosely constrained absorption $N_{\text{H},2} \sim 10^{23} \text{ cm}^{-2}$. The unfolded spectrum (Fig. 4) shows that the hotter component dominates the observed spectrum above ≈ 3 keV and

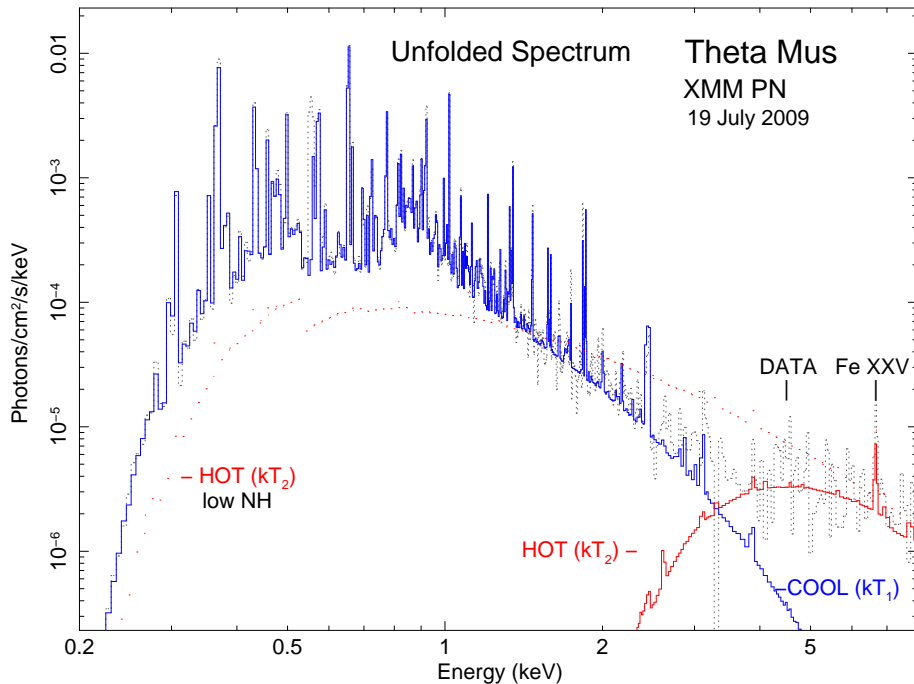


Figure 4. Unfolded *XMM-Newton* ObsId 0605670201 EPIC pn spectrum of θ Mus (gray dotted) showing cool and hot 2T *vps*shock model components (Table 2). The dotted red line shows the heavily absorbed hot component as it would appear if viewed under the same low absorption as the cool component.

accounts for the Fe XXV emission. But the crossover energy depends on the plasma temperatures and absorption column density. Factors affecting the absorption are discussed below (Sec. 6.4.1).

This absorbed hot component is strikingly similar to that derived from *XMM-Newton* observations of γ^2 Vel at low-state (Fig. 5 of Schild et al. 2004). Given the similarity it is likely that the hotter plasma originates in the CW interaction region near the line of centers where high temperatures and densities are expected. The key question is whether the CW region is in the SB system or the SB+OI system (Sec. 6.4.1).

RGS Grating Spectra. Although detailed analysis of the *XMM-Newton* RGS grating spectra is beyond the scope of this work, we briefly summarize key results. The RGS spectra (Fig. 3) are remarkably similar even though they were obtained five years apart at opposite phases. Low-energy lines down to C VI at $\lambda_{lab} = 33.734 \text{ \AA}$ were detected. The C VI RRC feature at 25.30 \AA is present in both spectra. Our analysis reveals that brighter lines are clearly broadened and redshifted in *both* observations with slightly higher shifts measured in the 2009 observation (Table 3). The strong O VIII line has width FWHM $\approx 1900 \pm 400 \text{ km s}^{-1}$ and is redshifted to $\approx +700 - +900 \text{ km s}^{-1}$. The O VIII line fluxes of the two observations differ by no more than $\approx 15\%$ suggesting that O VIII emission is nearly stable over 5 years.

The RGS spectra detect the O VII and Ne IX He-like triplets consisting of the closely-spaced resonance (*r*), intercombination (*i*), and forbidden (*f*) lines. In hot stars with strong UV radiation fields the line flux ratio $R = f/i$ is not a reliable electron density diagnostic but can constrain the line formation distance from the star and $G = (f + i)/r$ is temperature sensitive (Gabriel & Jordan 1969; Blumenthal, Drake, & Tucker 1972; Pradhan 1982; Porquet et al. 2001). The triplet components are well separated in O VII but not Ne IX. For the longer 2004 observation with highest signal-to-noise

ratio we obtain O VII flux ratios (normalizing the r line flux to unity) $r:i:f = 1.00:0.17:0.50$ giving $R = 3.0$ [2.0 - 4.9] and $G = 0.7$ [0.5 - 0.9]. The large uncertainty range for R is due to the uncertainty in measuring the flux of the faint i line. In the case of low collisional excitation where the electron density is much less than the critical density ($n_e \ll n_c$) and stellar photoexcitation is well below the critical photoexcitation rate ($\phi_* \ll \phi_c$) the limiting values for O VII are $R_o = 3.95$ and $G_o = 1.0$ (Pradhan 1982). Taking the uncertainty range of G into account a value $G < G_o$ is not ruled out. If $G < G_o$ the plasma is not in ionization equilibrium at the line formation temperature of O VII (Pradhan 1982). Sugawara et al. (2008) have argued for NEI conditions.

A lower limit on the O VII formation distance r_{OV} from the O6-7V star can be obtained using the lower bound on R as was done for γ^2 Vel (Skinner et al. 2001; Schild et al. 2004). The approach assumes the electron density is subcritical ($n_e \ll n_c$) and that photoexcitation is responsible for decreasing R to a value below R_o . Using the lower bound $R \geq 2.0$ for O VII gives a $R/R_o \geq 0.5$. Assuming $T_{eff} \approx 38,000$ K for the O6-7V star (Weidner & Vink 2010) and scaling the value of ϕ_*/ϕ_c in Table 2 of Blumenthal et al. (1972) for $T_{eff} = 10^5$ down to 38 kK gives a lower limit $r_{OV} \gtrsim 70 R_{OV}$. This bound is a first approximation and a more refined estimate would require detailed calculation of the stellar radiation fields. But it is clear that if photoexcitation dominates over collisions then the O VII triplet does not form close to the O6-7V star.

5.3. Summary of Spectral Analysis

The X-ray emission of θ Mus consists of a weakly-absorbed nearly steady cool component at $kT_1 \approx 0.4 - 0.7$ keV plus a hotter component at $kT_2 \gtrsim 4$ keV whose observed flux is variable on a timescale of ≤ 5 years. The hotter plasma contributed a greater fraction of the total X-ray flux at orbital phase $\phi \approx 0.65$ than at $\phi \approx 0.96$. Emission lines are broadened to $FWHM \geq 1000$ km s $^{-1}$ due to bulk plasma motion. Low-temperature emission lines are redshifted to velocities as high as $v \approx +800 - +900$ km s $^{-1}$. But no significant centroid shift was measured in *Chandra* HETG spectra of the S XV line which traces warmer plasma that would be located nearer to the line-of-centers in CW shock binaries. The strong O VII forbidden line in the 2004 *XMM-Newton* RGS spectrum can be explained if O VII forms in cool low-density plasma located far from the O6-7V star. The significant decline in hot component flux can be attributed to increased absorption of the hot component at phase $\phi \approx 0.95 - 0.98$ (WR in front). The θ Mus X-ray luminosity for the observations analyzed herein is $\log L_x(0.2 - 8 \text{ keV}) = 33.22 - 33.36$ ergs s $^{-1}$ (Table 2), close to the *Einstein* value $\log L_x = 33.2$ ergs s $^{-1}$. It is also similar to other massive WC binaries (Pollock 1987) including γ^2 Velorum ($\log L_x = 33.06 - 33.17$; Schild et al. 2004).

6. DISCUSSION

6.1. Comparison with γ^2 Velorum

The X-ray observations of θ Mus show some striking similarities with the 78-day WC8+O7.5 binary γ^2 Velorum studied by Willis, Schild, & Stevens (1995), Stevens et al. (1996), Skinner et al. (2001), and Schild et al. (2004). In addition to their similar spectral types both systems have a cool plasma component that is viewed under low absorption and appears to be nearly steady with orbital phase. The C VI RRC feature in both systems points to an extended region where carbon ions that likely originate in the WC star wind recombine with free electrons. Extended cool plasma located far out in the system is also implicated by strong forbidden lines in He-like triplets for both stars. In addition, hotter plasma including the Fe XXV line evidently viewed through high absorption at certain phases

is present, as expected for CW shock emission near the line-of-centers. Line broadening is detected in both systems with widths $\text{FWHM} \geq 1000 \text{ km s}^{-1}$. The X-ray luminosity of $\gamma^2 \text{ Vel}$ is similar to $\theta \text{ Mus}$. However, one notable difference is that the *low-temperature* X-ray emission lines of $\theta \text{ Mus}$ are redshifted but no significant line shifts have been detected in $\gamma^2 \text{ Vel}$ (Skinner et al. 2001). The unusual line shifts (or lack thereof) are not easily reconciled with colliding wind theory.

6.2. X-ray Emission from the O Stars

Although intrinsic X-rays from the WC6 star are not anticipated (Sec. 1) the X-ray emission of $\theta \text{ Mus}$ could include intrinsic emission from the OV or OI stars. As an example, soft emission from the O9III star $\theta \text{ Mus B}$ lying south of $\theta \text{ Mus}$ is faintly detected by *Chandra* (Fig. 1). X-ray grating observations of $\zeta \text{ Ori}$ (O9.7Ib) show cool plasma that is consistent with radiative wind shocks and heavily suppressed forbidden lines in O VII and Ne IX (Waldron & Cassinelli 2000; Raassen et al. 2008). The suppressed *f* lines imply cool plasma formation close to the star, clearly different from $\theta \text{ Mus}$. The $\zeta \text{ Ori}$ X-ray luminosity is $\log L_x = 32.14 \text{ ergs s}^{-1}$ (Raassen et al. 2008). If L_x of the O9.5I star in the $\theta \text{ Mus}$ system is similar then it would account for $<10\%$ of the observed value.

It is also unlikely that intrinsic O6-7V star emission alone can account for the observed L_x , the hotter plasma traced by the Fe XXV line, and the redshifted lines. Main sequence O-type stars are generally soft X-ray sources and a recent study based on *XMM-Newton* data and *Gaia* distances yields the correlation $\log(L_x/L_{bol}) = -6.6 \pm 0.4$ (Gómez-Morán & Oskinova 2018). Adopting a typical O6-7V value $\log(L_{bol}/L_\odot) = 5.65$ gives $L_x = 0.11$ (0.045 - 0.28) L_\odot or $\log L_x = 32.6$ (32.23 - 33.03) ergs s^{-1} which is less than the observed value $\log L_x = 33.3 \text{ ergs s}^{-1}$. Thus, intrinsic emission from the O stars could account for some, but not all, of the observed X-ray luminosity. But if the O-star contribution were due to radiative wind shocks then one would expect low-temperature lines to be blueshifted (not redshifted) and the presence of hot plasma in $\theta \text{ Mus}$ is at odds with radiative wind shock predictions.

6.3. Colliding Wind Predictions

The presence of redshifted *low-temperature* emission lines in $\theta \text{ Mus}$ at phase $\phi \approx 0.6$ when the OV star should be nearly in front of the WC star is unexpected if the cooler X-ray plasma arises between the WC and O star in the SB system (Sec. 2). As suggested by Sugawara et al. (2008) the redshifted lines could be reconciled with the CW interpretation if the CW shock lies between the SB system and the OI star lying further away in a bound orbit. But regardless of whether a CW shock is located in the wide SB+OI system or the SB system it is evident from the low absorption of cooler plasma, C VI RRC feature, and O VII *f/i* line ratio that some cool plasma is located far out in an extended region where the wind density is low. On the other hand the drop in flux of the hotter plasma component on a timescale of ≤ 5 years is compatible with the 19-day SB system but would be rather fortuitous if the SB+OI system period is significantly greater than 40 years. Below we compare CW predictions for SB system and the wide SB+OI system.

SB System. The location of the stagnation point on the line-of-centers between the WC6 and O6-7V stars is determined by the wind momentum ratios (eq. [1] of Stevens et al. 1992)

$$\left[\frac{\dot{M}_{WC} V_{WC}(r_1)}{\dot{M}_{OV} V_{OV}(r_2)} \right]^{1/2} = \frac{r_1}{r_2} \equiv \mathcal{R} \quad (1)$$

where r_1 and r_2 are the respective distances from the center of the WC and O stars to the stagnation point and $r_1 + r_2 = D$ is the binary separation. Mass loss parameters for WR and O stars are rather uncertain but for purposes of an estimate we adopt the WC6 mass loss rate $\log \dot{M}_{WC} = -4.74 M_\odot \text{ yr}^{-1}$ and terminal wind speed $V_{\infty,WC} = 2060 \text{ km s}^{-1}$ of Nugis & Lamers (2000). For the O6-7V star we assume $\log \dot{M}_{OV} = -6.3 M_\odot \text{ yr}^{-1}$ and $V_{\infty,OV} = 2450 \text{ km s}^{-1}$ (Lamers & Leitherer 1993). These adopted values give $\mathcal{R} = 5.5$ and place the stagnation point at the contact discontinuity close to the O6-7V star at $r_2 = 0.15D$. Using assumed masses $M_{WC6} = 12 M_\odot$ (Hill et al. 2002) and $M_{OV} = 30 M_\odot$ (Weidner & Vink 2010), the computed semi-major axis is $a = 0.49 \text{ AU} = 105 R_\odot$ for $P_{orb} = 19.1325 \text{ d}$. A slightly lower mass for the OV star is possible (Moffat & Seggewiss 1977) but would not significantly alter the computed value of the semi-major axis. Typical radii for WC6 stars are $R_{WC6} \approx 3 R_\odot$ (Sander et al. 2012) and for O7V stars $R_{OV} \approx 10 R_\odot$ (Lamers & Leitherer 1993). This gives $r_2 \approx 32 R_\odot \approx 3 R_{O7V}$. The above results assume the winds of both stars have reached terminal speed before colliding. This would be the case for the WC6 star assuming a typical hot star wind velocity profile $V(r) = V_\infty[1 - (R_*/r)]^\beta$ with $\beta \approx +0.7 - +1.0$ (Krtićka & Kubát 2011). But the O star wind would only be at about 70% of its terminal speed which would tend to push the stagnation point even closer to (or perhaps onto) the O star surface. Thus the hottest plasma would be located near the line-of-centers close to the OV star.

Theory provides analytic expressions for the CW shock X-ray luminosity ($L_{x,cw}$) that depend on mass loss parameters, binary separation, stellar radii, and whether the shock is adiabatic or radiative (e.g. Usov 1992; Stevens et al. 1992). But previous studies of WR+OB systems have not always yielded good agreement between the observed L_x and predictions (e.g. Skinner et al. 2019b). The discrepancies may be in part due to inaccurate mass loss rates resulting from inhomogeneous (i.e. clumped) winds (Cherepashchuk 1990; Zhekov 2012). Also for wide WR binaries where the winds have reached terminal speeds before colliding, theory predicts that $L_{x,cw}$ should scale inversely with orbital separation D . But no such change was detected in the hard-band X-ray emission of $\gamma^2 \text{ Vel}$ at two different orbital phases where D is thought to have changed (Schild et al. 2004). It thus seems that not all WR binaries faithfully adhere to the theoretical $L_{x,cw} \propto 1/D$ scaling relation.

For wide binaries with periods more than a few days the CW shock is expected to be adiabatic but for short-period systems it can be radiative. In the latter case most of the shock energy is radiated away (tending to increase $L_{x,cw}$) and the shocked plasma is nearly isothermal. A rough gauge on whether the shock is adiabatic or radiative is given by the ratio of the cooling time to escape time $\eta = t_{cool}/t_{esc}$ where $\eta \ll 1$ is typical for radiative shocks and $\eta \gtrsim 1$ for adiabatic shocks. The wide SB+OI system is clearly in the adiabatic regime but the close SB system could be either adiabatic or radiative. For the $\theta \text{ Mus}$ SB system we obtain $\eta \approx 1.3$ (eq. [8] of Stevens et al. 1992) which favors the adiabatic regime, but marginally so. However, if the WR wind shocks onto the surface of the O star companion then radiative cooling can be important even if $\eta > 1$ (Stevens et al. 1992).

If we assume, as suggested above, that the WC star wind impacts the surface of the O6-7V star (with the shock cone wrapping around it) then the CW luminosity predicted for an adiabatic shock (eq. [81] of Usov 1992) is more than an order of magnitude less than the observed L_x . But if the shock is radiative then (eq. [80] of Usov 1992)

$$L_{x,cw} = \frac{1}{8} \left[\frac{R_{OV}}{D} \right]^2 L_{wind,WC} \quad (2)$$

where the wind luminosity is $L_{wind,WC} = (1/2)\dot{M}_{WC}V_{\infty,WC}^2$ and we have assumed spherical homogeneous winds with mass density $\rho_{\infty} = \dot{M}_{WC}/(4\pi D^2 V_{\infty,WC})$. Using the same mass loss, stellar, and orbital parameters as above gives $\log L_{x,cw} = 33.8 \text{ ergs s}^{-1}$, or about +0.5 dex higher than observed. This difference could potentially be explained if the adopted WC mass loss rate is too high as may be the case if the wind is clumped. Thus if the WR wind shocks onto the O6-7V star the predicted $L_{x,cw}$ for a radiative shock is in better agreement with the observed value. Even so, the above $L_{x,cw}$ estimates are only approximate since the Usov (1992) formulation assumes a bremsstrahlung X-ray spectrum and does not account for line emission.

SB+OI System. A similar analysis to above can be carried out for the SB+OI system. Because of the much wider separation the CW shock would be adiabatic and the winds would be at terminal speeds before colliding. In Eq. (1) we assume that the combined SB wind is dominated by the powerful WC6 wind and use its wind speed and mass loss rate. For the OI wind we adopt $\dot{M}_{OI} = 3.2 \times 10^{-6} M_{\odot} \text{ yr}^{-1}$ and $V_{\infty,OI} = 1800 \text{ km s}^{-1}$ (Lamers & Leitherer 1993). For these wind parameters $\mathcal{R} = 2.55$ and the contact discontinuity lies closest to the OI star at an offset of $0.28D$. To estimate the deprojected separation D we assume an arbitrary angle of 45° between the line-of-sight and the major axis of the SB+OI system which gives $D = 141 \text{ AU}$. In that case the discontinuity is offset from the OI star along the line-of-centers by 40 AU. The predicted X-ray luminosity of the CW shock between the SB system and OI star is (summing results of eqs. [89, 95] of Usov 1992) $\log L_{x,cw} \approx 33.6 \text{ ergs s}^{-1}$ which is within a factor of two of the observed value for θ Mus. This is rather good agreement and an adiabatic CW shock in the SB+OI system could account for the observed L_x unless D is much greater than assumed above.

6.4. Questions and Challenges for the Colliding Wind Interpretation

6.4.1. Where is the Hot Plasma Located?

If the OI supergiant is in a long-period orbit around the SB system then two CW shock regions may be present: one in the SB system and another in the SB+OI system. If so their contributions would be superimposed in the X-ray spectra. This creates some ambiguity as to where the X-ray emission originates.

As we have shown, the cooler plasma is located in an extended region surrounding the θ Mus system. The redshifted lines in the cooler plasma component that show little change at opposite SB orbital phases can be explained if the cooler plasma originates in a CW shock in the wide SB+OI system with the OI star being further away (Sugawara et al. 2008). Even if the above picture is correct, it does not guarantee that the hottest plasma also originates in the SB+OI system. The key diagnostic of the hot plasma is the Fe XXV line at 6.67 keV. Unfortunately this line is not bright enough to obtain a reliable centroid measurement in the *Chandra* grating spectra and is not captured by *XMM-Newton* RGS. So we do not know if it is persistently redshifted, as are the lines tracing cooler plasma.

There are two clues pointing to the SB system as the source of the hotter plasma. One is the hard-band variability timescale of ≤ 5 years. This timescale is not problematic for the 19-day SB orbit but may be for the wide SB+OI system whose orbital period is not known but is certainly $\gtrsim 40$ years.

The second clue is the high absorption toward the hot component $N_{H,2} \sim 10^{23} \text{ cm}^{-2}$ inferred from fits of the 2009 EPIC spectrum. This value is similar to that determined for γ^2 Vel and was

attributed to a CW shock between the WC and OIII stars (Schild et al. 2004). CW theory predicts a characteristic absorption column density near orbital quadrature (Stevens et al. 1992)

$$N_{\text{H,cw}} \sim 5 \times 10^{22} \left[\frac{\dot{M}_{-6}}{V_{\text{wind},1000}} \right] \left[\frac{1 + \mathcal{R}}{\mathcal{R}} \right] D_{12}^{-1} \text{ cm}^{-2} \quad (3)$$

where \dot{M}_{-6} (units of $10^{-6} M_{\odot} \text{ yr}^{-1}$) and $V_{\text{wind},1000}$ (units of 1000 km s^{-1}) correspond to the dominant wind, \mathcal{R} is the wind momentum ratio of the dominant to weaker wind (eq. [1]) and D_{12} is the separation in units of 10^{12} cm . For the SB system $\mathcal{R} \approx 5.5$ and for the SB+OI system $\mathcal{R} \approx 2.55$, as computed above. The key discriminant is the separation D which is at least 100 times larger in the SB+OI system. That leads to a much smaller absorption estimate $N_{\text{H,cw}} \sim 10^{19.8} \text{ cm}^{-2}$ compared to the SB system $\sim 10^{22.6} \text{ cm}^{-2}$. The wind absorption is abundance dependent and will vary over the orbit as the line-of-sight through the wind interaction region changes. But the much larger characteristic value of $N_{\text{H,cw}}$ predicted for the SB system is clearly in better agreement with that needed to explain the decrease in hard-band flux in the 2009 *XMM-Newton* observation.

6.4.2. The Mystery of the Missing Blueshifted Lines

Even if the persistent redshifted low-temperature lines originate in a CW shock in the wide SB+OI system, that does not explain the absence of blueshifted lines near SB orbital phase $\phi \approx 0.5\text{-}0.6$ (OV star in front) where they should be seen if detectable CW emission emerges from the SB system. This is not the first time questions about undetected line shifts have arisen in massive WR binaries (Sec. 6.1). A few possible explanations for the no-show blueshifts are considered below, all being somewhat speculative.

If there were no *detectable* CW shock emission from the SB system then the observed X-ray emission would be entirely attributed to a CW shock in the long-period SB+OI system. If the OI star is in a bound orbit and $P_{\text{orb,OI}} \gg 40$ years then its orbital motion over the time interval of 18 years spanned by the X-ray observations might not be sufficient to cause line centroids to shift from red to blue. In fact no line shifts from red to blue were detected (Table 3) so a period $\gg 40$ years is consistent with the X-ray results. Obviously, if blueshifted lines are not expected then their absence is no longer a mystery. But in this picture the SB system would *not* contribute significantly to the X-ray emission and this would be quite exceptional if the WR companion is indeed a OV star. Other WC+O binaries are bright X-ray sources well above the detection limits of the observations discussed here (Pollock 1987). Also if the SB system were X-ray faint (or quiet) then the hot heavily-absorbed plasma would be attributed to the wide SB+OI system. But as shown above the high absorption needed to account for the decrease in hard-band flux is much greater than predicted by CW theory for the wide SB+OI system. We thus conclude that the hypothesis of no detectable CW X-rays from the SB system could explain the lack of blueshifted lines but it does not square well with what is known about X-ray emission of other WC+O binaries or CW theory absorption predictions.

Line centroid shifts originating in high-velocity shocked gas in the SB system would be difficult to detect if the SB orbit is viewed at low inclination (face-on) or if the shock cone opening angle is large and the flow velocity along the line-of-sight is small. But on the contrary optical radial velocity variations imply a rather high orbital inclination of at least $i \approx 49^\circ$ (Moffat & Seggewiss 1977; Lenoir-Craig et al. 2021). A wide shock cone with a half opening angle $\theta_{1/2} \approx 90^\circ$ would occur for nearly equal wind momenta $\mathcal{R} \approx 1$ (Stevens et al. 1992) and large adjustments in the assumed

mass-loss parameters would thus be required. But such a large opening angle is not consistent with the models of Hill et al. (2002) which gave $\theta_{1/2} = 46^\circ \pm 4^\circ$.

The accuracy of the SB system orbital ephemeris is crucial for calculation of orbital phases and interpreting line shifts. Determination of the SB orbital parameters for θ Mus is difficult (Sec. 2). The formal uncertainties in P_{orb} and reference HJD for minimum light T_o corresponding to $\phi = 0$ adopted here (Table 1) are too small to produce a substantial error in the computed phases of the X-ray observations. Combining the uncertainties for P_{orb} and T_o results in a phase error of $\Delta\phi \approx 0.08$ (1.54 d) for the June 2022 *Chandra* observations and only half that amount for the *XMM-Newton* observations. Even so, the X-ray phases are quite sensitive to the adopted period and a small error of 0.013 d in P_{orb} would shift the computed *Chandra* phases by $\Delta\phi \approx 0.25$. If the shorter periods obtained by Moffat & Seggewiss (1977) or Marchenko et al. (1998) were adopted the computed phases would change dramatically. But the upper limit on orbital period change $\dot{P}_{orb} < -4.57 \text{ s yr}^{-1}$ derived by Lenoir-Craig et al. (2021) has a negligible effect on computed X-ray phases. Additional X-ray observations with more complete phase coverage over the 19 day orbit would be useful to see if line shifts vary with phase or from red to blue. There is already a hint for slightly larger redshifts in the 2009 *XMM-Newton* RGS spectra than in 2004 (Table 3). Also any future observations that improve our knowledge of the θ Mus SB or wide SB+OI system orbital parameters or the nature of the elusive WR companion (discussed by Hill et al. 2002) might help clarify the X-ray results.

7. SUMMARY OF MAIN RESULTS

New *Chandra* X-ray observations of θ Mus confirm that emission lines in the cooler plasma component are redshifted near $\phi \approx 0.65$ (OV star passing in front of the WC star) as previously reported from 2004 *XMM-Newton* observations. An archived 2009 *XMM-Newton* observation reveals that low-temperature lines are similarly redshifted at opposite phase $\phi \approx 0.95$. The persistent redshifts could be attributed to a CW shock in the wide SB+OI system. But blueshifted lines that should appear if CW shock emission is also present in the short-period SB system have not been detected so far, for unknown reasons. Assuming no large changes occurred in the intrinsic X-ray spectrum of θ Mus, the decrease in emergent hard-band flux between the 2004 and 2009 *XMM-Newton* observations is likely due to increased absorption toward the hotter plasma component. The high absorption inferred from spectral fits points toward dense hot wind-shocked plasma near the line-of-centers in the confines of the SB system. The X-ray emission of θ Mus is quite similar to the WC+O binary γ^2 Vel implying a common physical mechanism and both systems show puzzling line centroid properties that are not easily reconciled with CW models.

This work was supported by *Chandra* award GO1-22006X issued by the Chandra X-ray Observatory Center (CXC). The CXC is operated by the Smithsonian Astrophysical Observatory (SAO) for, and on behalf of, the National Aeronautics Space Administration under contract NAS8-03060. This work is partially based on archival data obtained with *XMM-Newton*, an ESA science mission with instruments and contributions from ESA and the USA (NASA). This work has utilized HEASOFT developed and maintained by HEASARC at NASA GSFC and the *XMM-Newton* SAS data analysis software package.

This paper employs a list of *Chandra* datasets obtained by the *Chandra* X-ray Observatory contained in [DOI: 10.25574/cdc.173](https://doi.org/10.25574/cdc.173).

Facilities: *Chandra*; *XMM-Newton*

Software: CIAO (Fruscione et al. 2006), HEASoft (HEASARC 2014), XSPEC (Arnaud 1996), SAS (Gabriel et al. 2004)

REFERENCES

- Anders, E., & Grevesse, N. 1989, *GeoCoA*, 53, 197
- Arnaud, K.A. 1996, *Astronomical Data Analysis Software and Systems V*, eds, G. Jacoby & J. Barnes, ASP Conf. Series v. 101, 17
- Barlow, M.J., Smith, L.J., & Willis, A.J. 1981, *MNRAS*, 196, 101
- Blumenthal, G.R., Drake, G.W., & Tucker, W.H. 1972, *ApJ*, 172, 205
- Cassinelli, J.P., Miller, N.A., Waldron, W.L., MacFarlane, J.J., & Cohen, D.H. 2001, *ApJ*, 554, L55
- Cherepashchuk, A.M. 1976, *Sov. Astron. Letters*, 2, 138
- Cherepashchuk, A.M. 1990, *Sov. Astron.*, 34, 481
- Dougherty, S.M. & Williams, P.M. 2000, *MNRAS*, 319, 1005
- Feldmeier, A., Kudritzki, R.-P., Palsa, R., Pauldrach, A.W.A., & Puls, J. 1997, *A&A*, 320, 899
- Fruscione, A. et al. 2006, *Proc. SPIE*, 6270, id. 62701V
- Gabriel, C. et al. 2004, *Ast. Soc. of the Pac. Conference Series*, 314, 759
- Gabriel, A.H. & Jordan, C. 1969, *MNRAS*, 145, 241
- Gómez-Morán, A. & Oskinova, L.M. 2018, *A&A*, 620, A89
- Gorenstein, P. 1975, *ApJ*, 198, 95
- Hartkopf, W.J., Mason, B.D., Gies, D.R. et al. 1999, *AJ*, 118, 509
- Hill, G.M., Moffat, A.F.J., & St.-Louis 2002, *MNRAS*, 335, 1069
- Kahn, S.M. et al. 2001, *A&A*, 365, L312
- Krtićka, J. & Kubát, J. 2011, *A&A*, 534, A97
- Lamers, H.J.G.L.M. & Leitherer, C. 1993, *ApJ*, 412, 771
- Lenoir-Craig, G., St.-Louis, N., Moffat, A.F.J., & Pablo, H. 2021, *MNRAS*, 506, 4465
- Lucy, L.B. & White, R.L. 1980, *ApJ*, 241, 300
- Luo, D., McCray, R., & MacLow, M.-M. 1990, *ApJ*, 362, 267
- Marchenko, S.V. et al. 1998, *A&A*, 331, 1022
- Moffat, A.F.J. & Seggewiss, W. 1977, *A&A*, 54, 607
- Oskinova, L.M., Ignace, R., Hamann, W.-R., Pollock, A.M.T., & Brown, J.C. 2003, *A&A*, 402, 755
- Owocki, S.P., Castor, J.I., & Rybicki, G.B. 1988, *ApJ*, 335, 914
- Pollock, A.M.T. 1987, *ApJ*, 320, 283
- Porquet, D., Mewe, R., Dubau, J., Raassen, A.J.J., & Kaastra, J.S. 2001, *A&A*, 376, 1113
- Pradhan, A.K. 1982, *ApJ*, 263, 477
- Prilutskii, O.F. & Usov, V.V. 1976, *Sov. Astron.*, 20, 2
- Raassen, A.J.J., van der Hucht, K.A., Miller, N.A., & Cassinelli, J.P. 2008, *A&A*, 478, 513
- Sander, A., Hamann, W.-R., & Todt, H. 2012, *A&A*, 540, A144
- Schild, H., Güdel, M., Mewe, R., Schmutz, W., Raassen, A.J.J., Audard, M., Dumm, T., van der Hucht, K.A., Leutenegger, M.A., & Skinner, S.L. 2004, *A&A*, 422, 177
- Schnurr, O. 1999, Master's Thesis, Univ. of Heidelberg
- Skinner, S.L., Güdel, M., Schmutz, W., & Stevens, I.R. 2001, *ApJ*, 558, L113
- Skinner, S.L., Güdel, M., Schmutz, W., & Zhekov, S.A. 2006, *Ap&SS*, 304, 97
- Skinner, S.L., Zhekov, S.A., Güdel, M., Schmutz, W., & Sokal, K.R. 2010, *ApJ*, 139, 825
- Skinner, S.L., Zhekov, S.A., Güdel, M., Schmutz, W., & Sokal, K.R. 2012, *AJ*, 143, 116
- Skinner, S.L., Sokal, K.R., & Güdel, M. 2019, *ApJ*, 871, 116
- Skinner, S.L., Zhekov, S.A., Güdel, M., & Schmutz, W. 2019b, *AN*, 340, 50
- Sokal, K.R., Skinner, S.L., Zhekov, S.A., Güdel, M., & Schmutz, W. 2010, *ApJ*, 715, 1327
- Stevens, I.R., Blondin, J.M., & Pollock, A.M.T., 1992, *ApJ*, 386, 265
- Stevens, I.R. et al. 1996, *MNRAS*, 283, 589
- St.-Louis, N., Drissen, L., Moffat, A.F.J., Bastien, P. & Tapia, S. 1987, *ApJ*, 322, 870
- Sugawara, Y., Tsuboi, Y., & Maeda, Y. 2008, *A&A*, 490, 259
- ud-Doula, A. & Owocki, S.P. 2002, *ApJ*, 576, 413
- Usov, V.V. 1992, *ApJ*, 389, 635
- van der Hucht, K.A. 2001, *NewAR*, 45, 135
- van der Hucht, K.A., Cassinelli, J.P., & Williams, P.M. 1986, *A&A*, 168, 111
- Vuong, M.H., Montmerle, T., Grosso, N. et al. 2003, *A&A*, 408, 581
- Waldron, W.L. & Cassinelli, J.P. 2000, *ApJ*, 548, L45

Weidner, C. & Vink, J.S. 2010, *A&A*, 524, A98
Willis, A.J., Schild, H., & Stevens, I.R. 1995,
A&A, 298, 549
Wosley, S.E. & Bloom, J.S. 2006, *ARA&A*, 44,
507

Zhekov, S. 2007, *MNRAS*, 382, 886

Zhekov, S. 2012, *MNRAS*, 422, 1332